Engineering Fracture Mechanics Vol. 31, No. 3, pp. 451–461, 1988
Printed in Great Britain.

0013-7944/88 $3.00 + .00

INTEGRATED EXPERIMENTAL-FINITE ELEMENT APPROACH FOR STUDYING ELASTO-PLASTIC CRACK-TIP FIELDS

T. V. HAREESH and F. P. CHIANG
Laboratory for Experimental Mechanics Research, S.U.N.Y. at Stony Brook, NY 11794-2300, U.S.A.

Abstract—A coupled Moiré-finite element method is used to calculate displacement and strain fields around a elasto-plastically deformed crack tip. This hybrid approach is shown to be economical when compared with conventional iterative finite element procedures from the point of view of computational time and storage when analysing problems involving extensive plastic deformations. By supplying surface deformation boundary conditions, one could determine field quantities in the interior of the material. Hybrid method gives more accurate field descriptions than regular finite element schemes.

1. INTRODUCTION

HYBRID methods are well known for studying mechanics problems which cannot be tackled efficiently by either experimental or numerical methods alone. It generally involves obtaining boundary conditions from experiments and using them in numerical models. This approach has been taken earlier by several investigators. Rao[1] used experimentally obtained temperature and surface traction data to solve for stresses inside an axisymmetric solid. Three dimensional photoelasticity data has been used by Barishpolsky[2] in solving elasticity problems. Balas *et al.*[3] have used holography with boundary element method while Moshley and Ranson[4] employed laser speckle interferometry to supply displacement boundary conditions in their hybrid analysis. Recently, Weathers *et al.*[5] have demonstrated the use of combined laser speckle photography and finite element method (FEM) to study stresses in a compressed disk. MacBain[6] has employed time average holography data to simulate plate vibrations numerically. The novel approach of using experimentally obtained load line displacement data in their FE model have let Kanninen *et al.*[7] and Shih *et al.*[8] to simulate field parameters ahead of a growing crack in a hardening material. Segalman *et al.*[9], have shown the applicability of a hybrid scheme for differenting experimental data for determining full-field strain distributions. Also, there have been attempts to use this method to make dynamic fracture study more plausible. In his survey article on hybrid stress analysis techniques, Kobayashi[10] has reviewed the progress in this field in the recent years.

In this paper, we demonstrate a hybrid method for studying elasto-plastic displacement and strain fields around a crack tip using Moiré technique in conjunction with FEM. Experimental surface displacement measurements are used to calculate the interior displacement and strain fields around a plastically deformed crack tip.

Unlike linear analysis, elasto-plastic analysis using FEM involves iterative schemes for seeking the solution. The number of iterations is a direct function of the extent of plastic deformation. This makes numerical modelling of material non-linearity problems massive in computational time and storage requirements. Analysing crack tip fields by FEM poses an additional difficulty due to the fine discretization required around the crack tip for precise displacement and strain field predictions. Also, since the field parameters around the immediate crack tip vicinity are three dimensional in nature, it calls for 3D FE analysis which is computationally very demanding. Under such circumstances it is very attractive to use a hybrid model for analysis. Here, an integrated Moiré-finite element analysis is presented for analysing crack tip fields in a single edge notch (SEN) sample made of a low hardening aluminum. Prior to implementing the hybrid model for this purpose, correctness of the nonlinear finite element code is tested by solving for strain concentration factor due to a circular hole in a uniformly stressed thin infinite sheet.

2. FINITE ELEMENT MODEL

Finite element model used in this study is based on small strain approximation and deformation theory of plasticity. The initial-stress method[11] is followed to continuously update the load matrix. The material stress–strain curve is experimentally obtained from a tensile test and stored in numerical form. This is used to calculate secant modulus (E_s) using the current effective strain in the element. Once secant modulus is known, elemental stiffness matrix is modified and load matrix is updated. Two types of FE models namely, 2D and 3D, have been used. 2D plane stress model uses isoparametric quadrilateral element with four nodes per element and two degrees of freedom per node corresponding to displacements in the x- and y-directions. The 3D model uses eight node linear brick elements with three degrees of freedom per node corresponding to displacements in x-, y- and z-directions. Numerical integration is performed at four and eight guassian locations in the 2D and 3D models, respectively.

In a linear finite element analysis (FEA), system of equations at the elemental level such as,

$$[k^e]\{\delta^e\} = \{f^e\} \tag{1}$$

where $[k^e]$ is the element elastic stiffness matrix, $\{\delta^e\}$ is the vector of nodal displacements and $\{f^e\}$ is the vector of nodal forces of the element are solved. Assembling each of these elemental quantities provides the global system of equations,

$$[k]\{\delta\} = \{f\} \tag{2}$$

which are to be solved for the unknown nodal displacements $\{\delta\}$. The elastic stiffness matrix $[k]$ is calculated using the strain–stress relation,

$$\{\epsilon\} = [D]\{\sigma\}$$

which assumes the form,

$$\begin{Bmatrix} \epsilon_x \\ \epsilon_y \\ \gamma_{xy} \end{Bmatrix} = \begin{bmatrix} 1/E & -\nu/E & 0 \\ -\nu/E & 1/E & 0 \\ 0 & 0 & 1/G \end{bmatrix} \begin{Bmatrix} \sigma_x \\ \sigma_y \\ \tau_{xy} \end{Bmatrix} \tag{3}$$

for plane stress and

$$\begin{Bmatrix} \epsilon_x \\ \epsilon_y \\ \epsilon_z \\ \gamma_{xy} \\ \gamma_{yz} \\ \gamma_{zx} \end{Bmatrix} = \begin{bmatrix} 1/E & -\nu/E & -\nu/E & 0 & 0 & 0 \\ -\nu/E & 1/E & -\nu/E & 0 & 0 & 0 \\ -\nu/E & -\nu/E & 1/E & 0 & 0 & 0 \\ 0 & 0 & 0 & 1/G & 0 & 0 \\ 0 & 0 & 0 & 0 & 1/G & 0 \\ 0 & 0 & 0 & 0 & 0 & 1/G \end{bmatrix} \begin{Bmatrix} \sigma_x \\ \sigma_y \\ \sigma_z \\ \tau_{xy} \\ \tau_{yz} \\ \tau_{zx} \end{Bmatrix} \tag{4}$$

in 3D case. Here E is the Young's modulus, ν is Poisson's ratio and G is shear modulus of the material. To perform elasto-plastic analysis, deformation theory of plasticity is used in the form,

$$\epsilon_{ij}^p = \frac{3}{2}\frac{\epsilon_e^p}{\sigma_e} s_{ij} \tag{5}$$

where s_{ij} is the stress deviator of σ_{ij} and ϵ_e^p and σ_e are the effective plastic strain and effective total stress. Using the value of secant modulus (Fig. 1a) E_s, the relation between the plastic strain vector $\{\sigma^p\}$ and stress vector $\{\sigma\}$ can be written as,

$$\{\epsilon^p\} = [P]\{\sigma\} \tag{6}$$

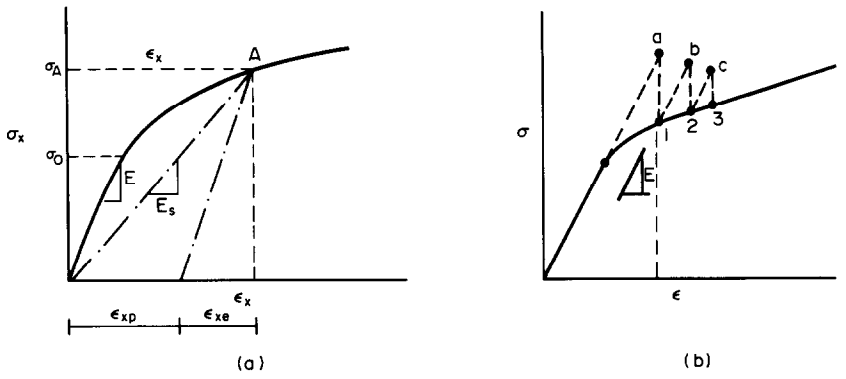

Fig. 1. (a) Secant modulus E_s from the stress–strain curve. (b) Initial stress method.

where $[P]$ is given by,

$$[P]=\frac{E-E_s}{EE_s}\begin{bmatrix} 1 & -1/2 & -1/2 & 0 & 0 & 0 \\ -1/2 & 1 & -1/2 & 0 & 0 & 0 \\ -1/2 & -1/2 & 1 & 0 & 0 & 0 \\ 0 & 0 & 0 & 3 & 0 & 0 \\ 0 & 0 & 0 & 0 & 3 & 0 \\ 0 & 0 & 0 & 0 & 0 & 3 \end{bmatrix}.$$

The above matrix $[P]$ can be reduced in 2D plane stress case by simply setting $\sigma_z = \gamma_{zx} = \gamma_{yz} = 0$.

The elasto-plastic analysis is implemented as follows: To begin with it is assumed that the entire region under study is deforming elastically and displacements are solved using eq. (2). Then, Von Mises yield criteria is invoked to check the yielding in each of the elements at their gauss points by comparing yield strain ϵ_0 with effective strain ϵ_e given by.

$$\epsilon_e=\frac{\sqrt{2}}{2(1+\nu')}\left[(\epsilon_x-\epsilon_y)^2+(\epsilon_y-\epsilon_z)^2+(\epsilon_z-\epsilon_x)^2+\frac{3}{2}(\gamma_{xy}^2+\gamma_{yz}^2+\gamma_{zx}^2)\right]^{0.5} \tag{7}$$

where ν' is equal to ν in the elastic range and 0.5 after yielding. For every plastically yielded element the modified elemental stiffness matrix $[k_s^e]$ is obtained using the relation,

$$\{\epsilon\}=\{[P]+[D]\}\{\sigma\}. \tag{8}$$

If $[k_r^e]=[k^e]-[k_s^e]$, then global system of equations can be expressed as,

$$[k]\{\delta\}_{i+1}=\{f\}+\sum\{r\}_i \tag{9}$$

where

$$\{r\}_i=\{k_r^e\}_i\{\delta^e\}_i.$$

This iterative procedure is shown schematically in Fig. 1(b).

A finite element code was developed based on the above algorithm. To test its correctness, the well known problem of a circular hole in a uniformly stressed infinite plate was chosen. The material characteristics correspond to that of Al 6061-T6 (Youngs modulus $E = 700\ \text{kg/mm}^2$; yield stress $\sigma_0 = 28\ \text{kg/mm}^2$; slope of the post yield stress–strain curve $m \approx 0.005\ \text{kg/mm}^2$). Figure 2 shows the finite element model of this problem. For an applied stress of $\sigma = \sigma_\infty/\sigma_0 = 0.9$,

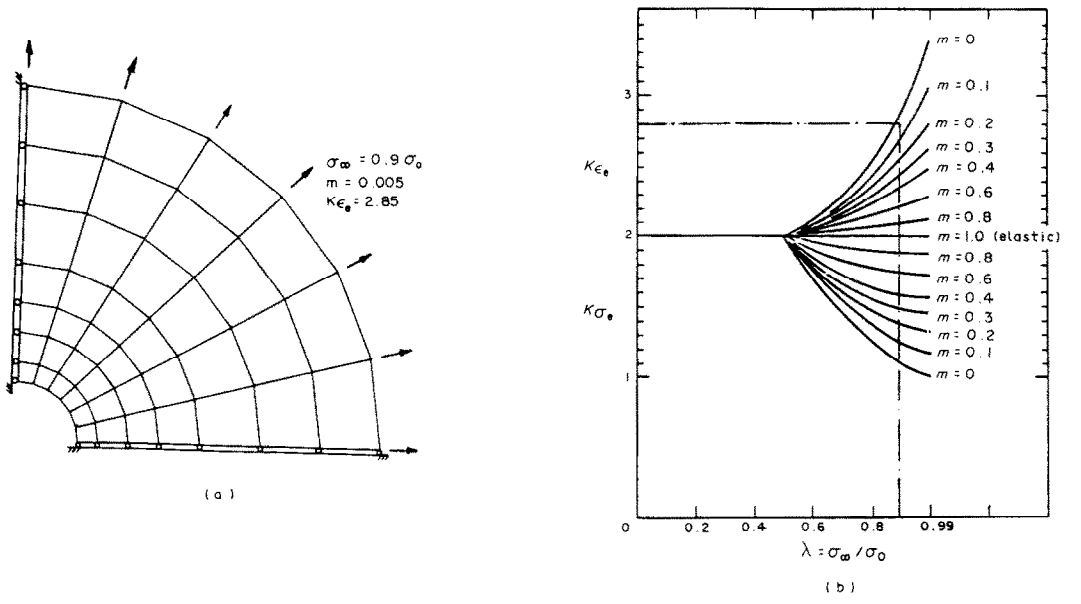

Fig. 2. Finite element model of circular hole in a thin plate subjected to uniform far field stress. (b) Strain conc. factor reported in [12].

the effective strain concentration factor at the hole boundary turned out to be 2.82 which is in good agreement (Fig. 2b) with the value reported by using the method of successive elastic solutions in [12]. The convergence criterion used was gauss point effective strain variation of less than 1% yield strain per iteration.

3. EXPERIMENTAL-NUMERICAL ANALYSIS

A combined experimental-numerical model was used to study displacement and strain fields in the crack tip vicinity of a SEN specimen. The specimen had an electro-discharge machined edge notch 12.5 mm long and 500 μm wide in a 3.2 mm thick sheet.

In-plane Moiré was used to get displacement fields around the crack tip. A 40 lines/mm cross grating, with its principal directions coinciding with the x- and y-coordinates, was photoprinted on the Al 6061-T6 specimen. The specimen was subjected to a far field tensile force equivalent to 80% of the yield stress of the material. The photoprinted grating on the specimen surface was photographed before (undeformed grating) and after (deformed grating) loading. Subsequent spatial filtering[13] of superimposed pair of undeformed and deformed recordings gives u and v displacement maps corresponding to deformations in x- and y-directions, respectively. Figure 3 shows the u and v fringe patterns thus obtained. Each of the fringes represents a displacement of 25 μm in the respective direction. They are governed by the equations of geometric Moiré, namely,

$$u_i = N_i p \text{ where } N_i = 0, \pm 1, \pm 2, \ldots \text{ and } i = 1, 2 \text{ with } u_1 = u,\ u_2 = v. \tag{10}$$

By numerically differentiating the above displacement fields using smoothed cubic spline approximations[14], displacement gradients with respect to the spatial co-ordinates x and y can be calculated. Strains were calculated using small strain-displacement relations, namely,

$$\epsilon_x = \left(\frac{\partial u}{\partial x}\right), \quad \epsilon_y = \left(\frac{\partial v}{\partial y}\right), \quad \gamma_{xy} = \left(\frac{\partial v}{\partial x}\right) + \left(\frac{\partial u}{\partial y}\right). \tag{11}$$

Next, a finite element model of the SEN specimen geometry was prepared (Fig. 4). Due to the symmetry of the problem, only one half of the plate was considered. The entire region R was divided into subdomains R_1 and R_2. Region R_1 consists of a mesh of fine elements around the

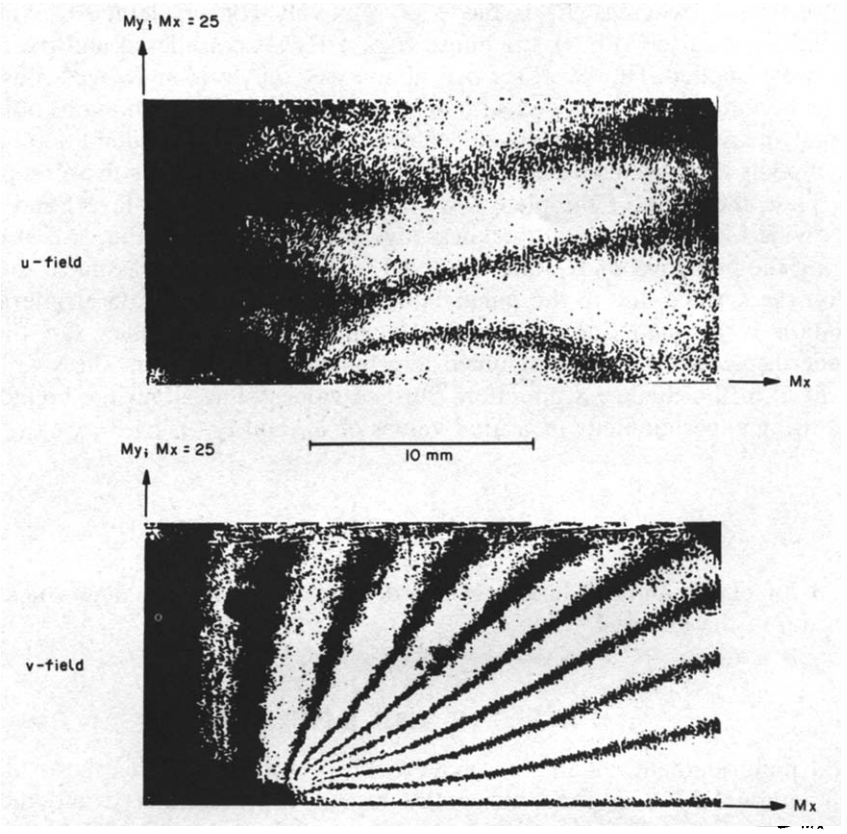

Fig. 3. u And v displacement maps around the notch tip of the SEN specimen subjected to uniaxial tension $\sigma_\infty = 0.8\sigma_0$.

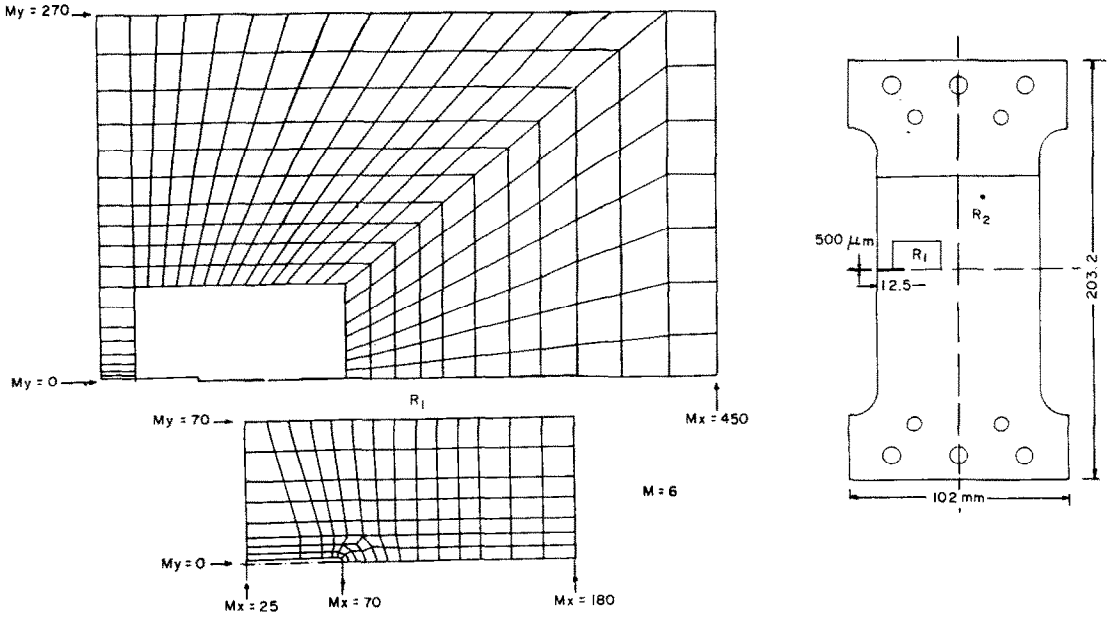

Fig. 4. Finite element model of the SEN specimen used.

strain concentration whereas R_2 is made of relatively coarse elements. While conducting conventional FE Analysis (FEA), the entire region R was considered and the force boundary conditions were applied. However, for hybrid analysis, only region R_1 was considered and the nodes on its boundary were supplied with displacement boundary conditions obtained from the experimental measurements. For all 2D calculations, plane stress conditions were assumed. When 3D models were used, two different types were considered. Firstly, a simpler model with the entire plate thickness of the plate forming one element (single layer) and the other with thickness divided into eight equal thickness layers (multi-layer). In the case of multi-layer 3D model, along the boundary of R_1, interior nodal displacements were assumed to be the same as the ones on the surface due to the unavailability of experimental data at interior nodes. This approximation is justified and surface displacements are negligible. On the other hand, out-of-plane displacement w was assumed to a linear function of thickness with the nodes on midplane fixed in the thickness direction. Surface values of w along the boundary of R_1 was calculated using experimentally measured values of ϵ_{xx} and ϵ_{yy} using,

$$\frac{2w}{h} \approx \epsilon_z = -c[\epsilon_x + \epsilon_y]$$

where $c = 1$ for plastic and $\nu/1-\nu$ for elastic deformations. h Is the plate thickness and ν the Poisson's ratio of the material.

4. RESULTS AND DISCUSSIONS

Several finite element calculations have been performed for the shown SEN geometry. When conventional FEA is done, the entire region R is considered and the nodal forces equivalent to $\sigma_\infty = 0.8\sigma_0$ was specified. For hybrid models, only region R_1 was considered and the nodes on the boundary were supplied with experimental displacement data. Two FE models, one a simple two dimensional plane stress model and the other a single layer three dimensional model were used. Hybrid models consisted of a 2D plane stress model, a 3D single layer model and a 3D multi-layer model. The v displacement and ϵ_y strains obtained by each one of these were compared with experimentally measured values. Figures 5 and 6 show that comparisons of displacement and strain contours. In these, magnification factor M is 6 and results are shown in a rectangular region around the crack tip (located at $(Mx) = 70$; $(My) = 0$ mm). All the calculations were performed on VAX 8600 multi-user facility and convergence occurred after about 125 iterations. Two dimensional FEA involved 762 degrees of freedom whereas 3D single layer FEA has 2286 d.o.f. On the other hand, 2D hybrid model used only 268 d.o.f., 3D single layer hybrid model 804 d.o.f. and 3D eight layer hybrid model had 2235 d.o.f. CPU time comparison between respective 2D and 3D models was approximately ten times favorable to hybrid models. Also, in Figs 5 and 6, the results from HRR equations[15–17] are shown. These were calculated by characterizing Al 6061-T6 stress-strain curve using Ramberg–Osgood type of approximation, namely,

$$\frac{\epsilon}{\epsilon_0} = \frac{\sigma}{\sigma_0} + \sigma\left[\frac{\sigma}{\sigma_0}\right]^n$$

where n is the hardening index, α is the material constant, σ_0 and ϵ_0 are the reference stress and strain, respectively.

Each of the displacement contours in Fig. 5 represent a displacement of 25 μm whereas strains are cumulative in steps of 0.004. To compare the relative accuracy of the different models with respect to experimental measurements, plots of ϵ_y along x-axis $[(Mx), (My) = 0]$ and normalized v displacement along (My) at $(Mx) = 100$ mm are shown in Fig. 7(a) and (b). From these, it is evident that hybrid models agree better with the experimental results than their counterpart finite element models. Three dimensional hybrid model improves the 2D hybrid model, particularly near the crack tip, since it accounts for the three dimensional effects[18, 19] that are known to dominate the near vicinity of a plastically deformed crack tip.

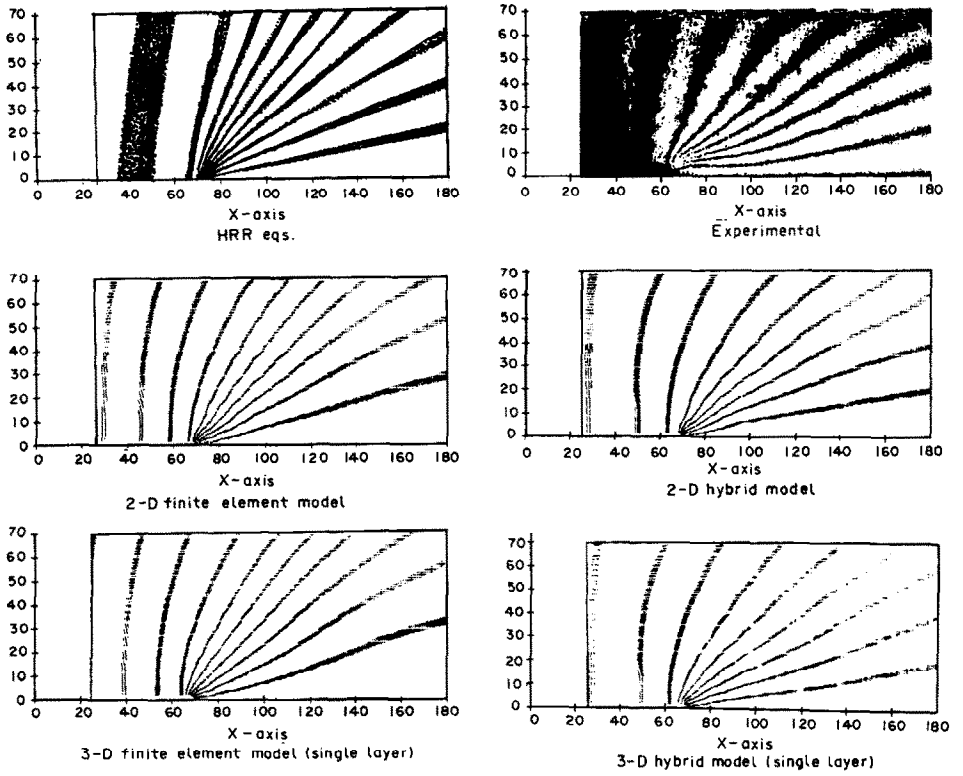

Fig. 5. Comparison of v displacement fields around the crack tip.

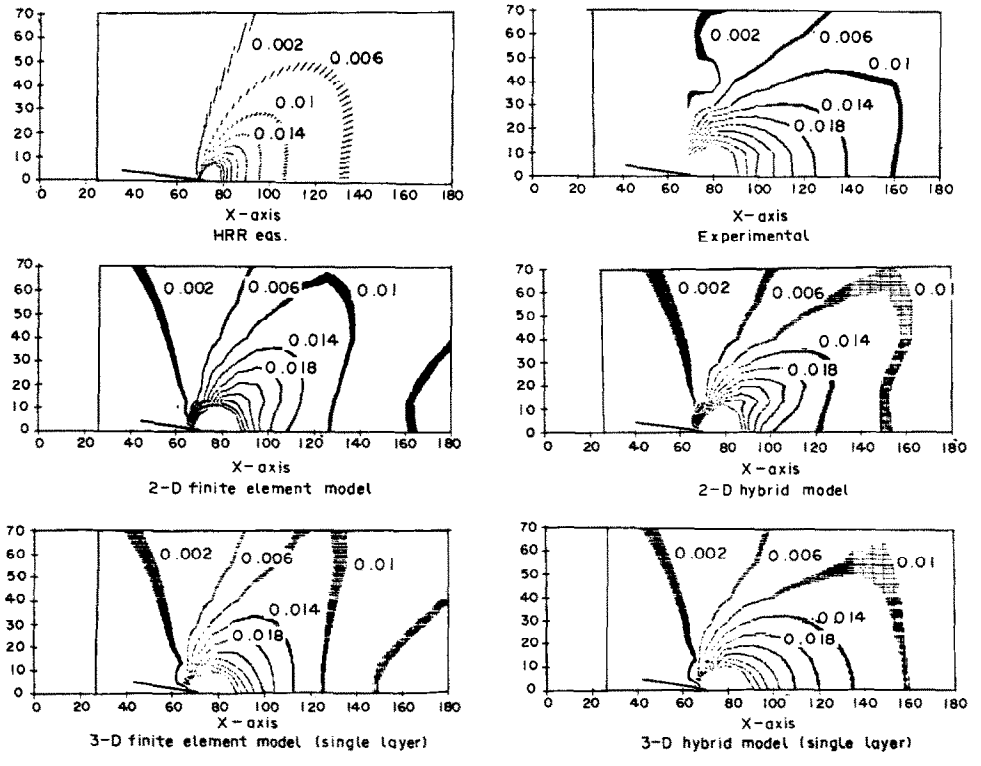

Fig. 6. Comparison of ϵ_y strain fields around the crack tip.

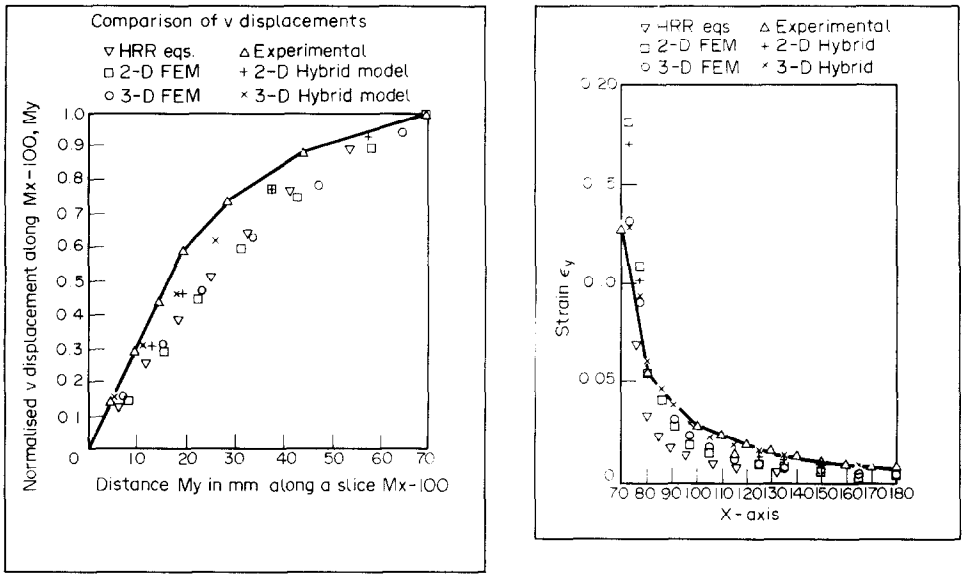

Fig. 7. (a) Comparison of v displacements along $Mx = 100$ mm and My where $M = 6.0$. (b) Comparison of strain ϵ_y along $(Mx, My = 0)$.

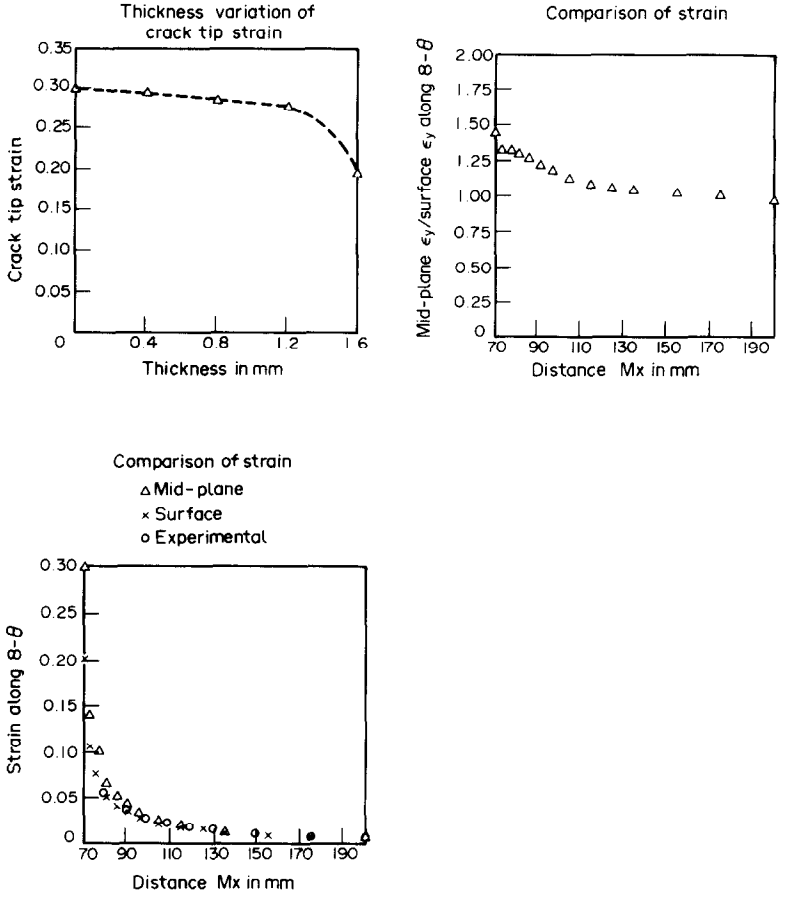

Fig. 8. (a) Surface and midplane ϵ_y along x-axis obtained from 3D multilayered hybrid model. (b) Ratio of midplane to surface strain ϵ_y ahead of the crack tip. (c) Thickness variation of crack tip strain ϵ_y.

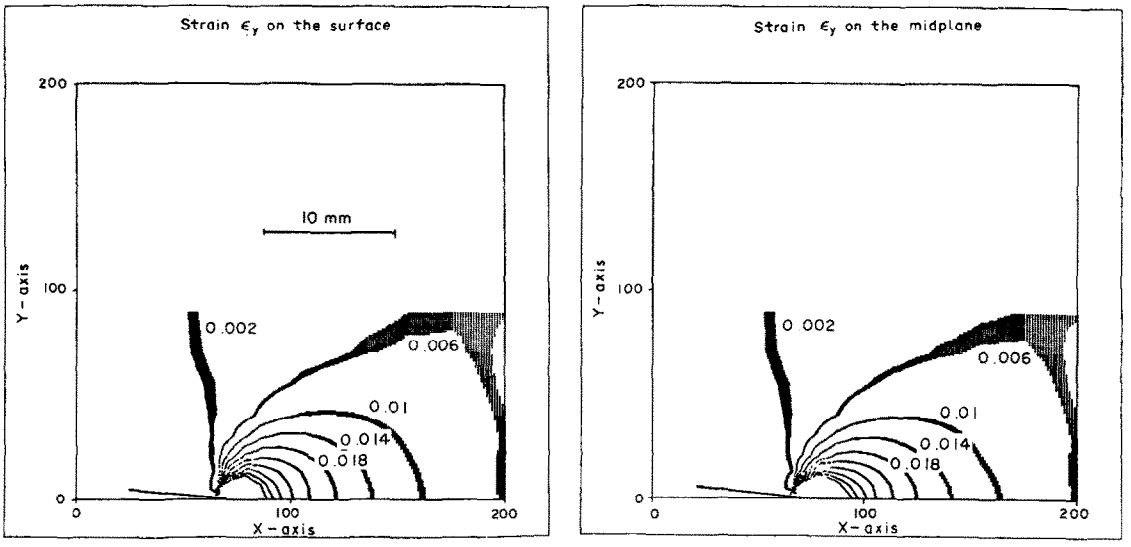

Fig. 9. Midplane and surface strain contours of ϵ_y.

Next, a multi-layer 3D hybrid model was used to determine the interior displacements and strains using experimental surface displacement boundary conditions at the nodal points. In Fig. 8(a) and (b) strain ϵ_y at the surface and the midplane along x-axis of the subdomain R_1 are plotted. Since the specified inplane nodal displacement at the boundary nodes are identical for both surface surface and interior nodes, the calculated values of strains tend to be the same at the boundary which they deviate significantly near the crack tip. The ratio of the midplane ϵ_y to surface ϵ_y drops from approximately 1.35 at the crack tip to 1 at the boundary. Thickness variation of crack tip strain ϵ_y is plotted in Fig. 8(c) which has a variation from 30% at the

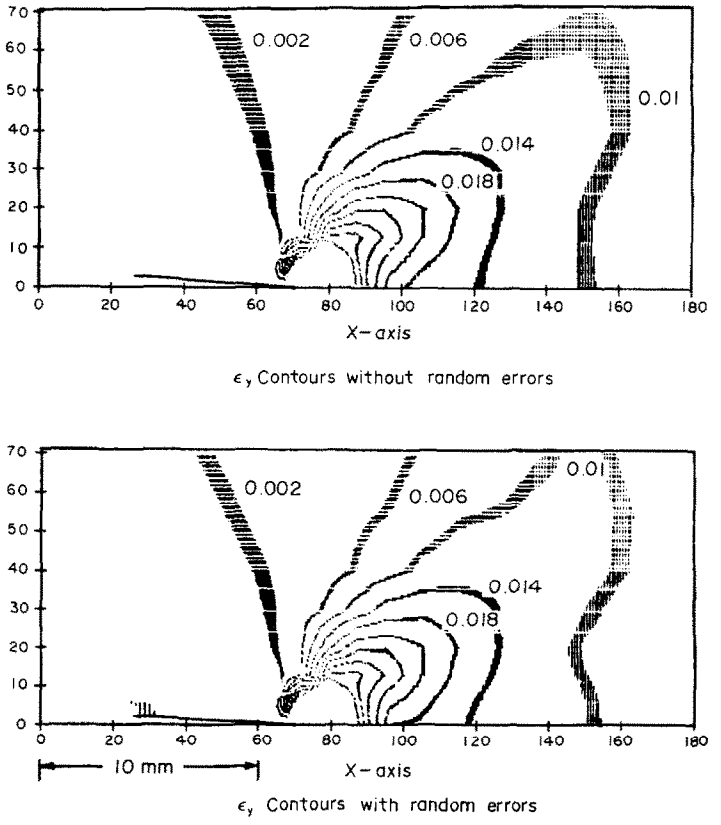

Fig. 10. Effect of $\pm 0.075p$ random error imposed on the measured displacement conditions.

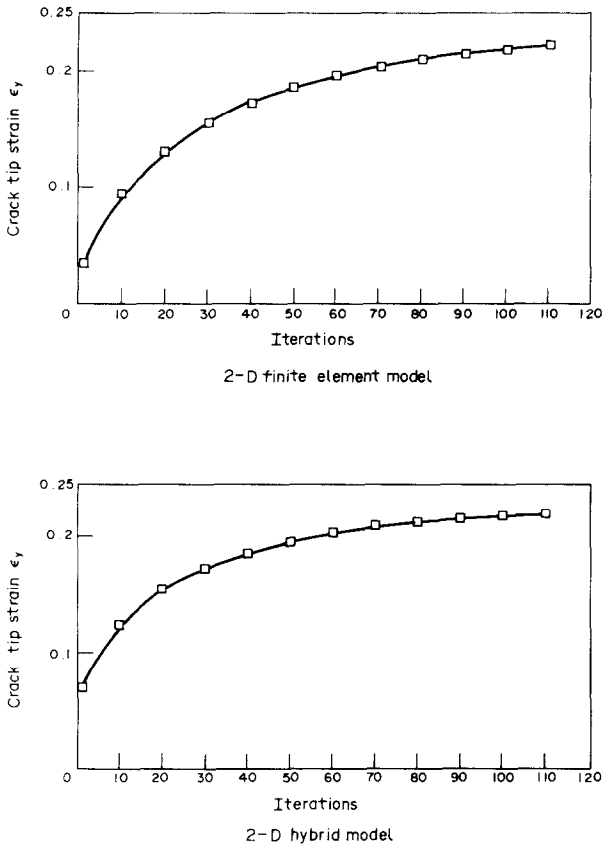

Fig. 11. Convergence of crack tip strain ϵ_y as a function of the number of iterations in 2D hybrid model and 2D FE model.

midplane to about 20% at the surface. In Fig. 9 ϵ_y strain contours around the crack tip for the midplane and surface are shown. Because of the identical far field boundary conditions in both the planes, the contours look similar near the boundary but the magnitudes of strain at points near the crack tip vicinity are quite different.

Lastly, to study the effect of experimental errors on the results obtained from hybrid models, calculations were performed using the 2D hybrid model used in the case of the SEN sample. A randomly generated error of ± 0.075 times the pitch of the grating was added to the experimental measurements at the nodal points. Figure 10 shows the effect of these imposed errors on the calculations shown as ϵ_y contours. The effects of the errors is clearly concentrated at the boundary where the displacements were specified whereas near the notch tip the strain contours are unchanged showing the stability of the hybrid formulations to boundary perturbations. Figure 11 shows the crack tip strain convergence achieved by the 2D hybrid and FE models.

5. CONCLUSIONS

We have successfully demonstrated a combined experimental numerical procedure for calculating the displacement and strain fields in the near vicinity of a plastically deformed crack tip in a work hardening material. This method is shown to be efficient in computer storage and processing time requirements when compared to conventional finite element calculations. A ten fold computer processing time savings can easily be achieved using the hybrid models. Because the boundary conditions for the hybrid methods are directly obtained from experiments, they also provide a better discription of the information around the crack tip.

By using suitable 3D hybrid models, three dimensional effects near the crack tip can also be accounted for while the same is only approximated by the two dimensional models. Multi-layer 3D hybrid modelling has shown a most interesting feature of this approach. By supplying the

experimental surface displacement boundary conditions, one could successfully calculate the interior field quantities.

It has been shown that the hybrid models are stable systems and that the errors in the experimental boundary conditions only affect the results near the boundary leaving the crack tip calculations unperturbed.

Acknowledgements—This work is supported by ONR Mechanics Division (Dr Y. Rajapkse, Scientific Officer) Contrac: No. N0001482K0566 and NSF Solid and GeoMechanics Program (Dr K. Thirumalai, Program Director) Grant No. MEA8403912.

REFERENCES

[1] G. V. Rao, Experimental–numerical hybrid techniques for body force and thermal stress problems-applications in power industry. *Proc. Joint Conf. Exp. Mech.* SESA, pp. 398–404 (1982).
[2] B. M. Barishpolsky, Development of a combined experimental and numerical method for the thermoelastic analysis. *Proc. SESA Spring Meeting* (1981).
[3] J. Balas, J. Sladek and M. Drzik, Stress analysis by combination of holographic interferometry and boundary integral method, *Exp. Mech.* **23**, 196–202 (1983).
[4] F. A. Moshley and W. F. Ranson, Laser speckle interferometry and boundary integral techniques in experimental stress analysis. *Developments in Theoretical and Applied Mechanics* (Edited by J. E. Stoneking), X, pp. 473–492. The Univ. of Tennessee (1980).
[5] J. M. Weathers, W. A. Foster, W. F. Swinson and J. L. Turner, Integration of laser speckle and finite element techniques of stress analysis. *Exp. Mech.* 60–85 (March 1985).
[6] J. C. MacBain, Displacement and strain of vibrating structures using time average holography. *Exp. Mech.* **18**, 361–372 (1978).
[7] M. F. Kanninen, E. F. Rybicki, R. B. Stonesifer, D. Broek, A. R. Rsoenfield, C. W. Marschall and G. T. Hahn, Elastic–plastic fracture mechanics for two dimensional stable crack growth and instability problems. *Elastic–Plastic Fracture* (Editied by J. D. Landes, J. A. Begley and G. A. Clarke), *ASTM STP* **668**, 121–150 (1979).
[8] C. F. Shih, H. G. deLorenzi and W. R. Andrews, Studies on crack initiation and stable crack growth. *Elastic–Plastic Fracture* (Edited by J. D. Landes, J. A. Begley and G. A. Clarke), *ASTM STP* **668** 65–120 (1979).
[9] D. J. Segalman, D. B. Woyak and R. E. Rowlands, Smooth spline like finite element differentiation of full-field experimental data over arbitrary geometry. *Exp. Mech.* 429–437. (December 1979).
[10] A. S. Kobayashi, Hybrid experimental–numerical stress analysis. *Exp. Mech.* 338–347 (Sept. 1983).
[11] R. D. Cook, *Concepts and applications of finite element analysis*, Second edition. John Wiley and Sons (1981).
[12] I. S. Tuba, Elastic–plastic stress and strain concentration factors at a circular hole in a uniformly stressed infinite plate. *J. appl. Mech.* **32**, 710–711 (1965).
[13] F. P. Chiang, Techniques of optical spatial filtering applied to the processing of Moiré fringe patterns. *Exp. Mech.* **6** 523–526 (1979).
[14] D. G. Berghaus and J. P. Cannon, Obtaining derivatives from experimental data using smoothed-spline functions. *Exp. Mech.* **13**, 38–42 (1973).
[15] J. W. Hutchinson, Singular behavior at the end of a tensile crack in a hardening material. *J. Mech. Phys. Solids* **16**, 13–31 (1968).
[16] J. W. Hutchinson, Plastic stress and strain fields at a crack tip. *J. Mech. Phys. Solids* **16**, 337–347 (1968).
[17] J. R. Rice and G. F. Rosengren, Plane strain deformation near a crack tip in a power law hardening material. *J. Mech. Phys. Solids* **16**, 1–12 (1968).
[18] F. P. Chiang and T. V. Hareesh, Three dimensional crack tip deformation: an experimental study and comparison to HRR field. College of Engng and Applied Sciences, SUNY at Stony Brook, NY, *Tech. Report* 481 (1986); to appear in the *Int. J. Fracture Mech.* (1988).
[19] J. C. Olinkiewicz, T. V. Hareesh and F. P. Chiang, 3-D deformation of surface notches in aluminum specimens. *SPIE Proc.* **814**, *Intl. Conf. on Photomechanics and Metrology*, San Diego, CA (August, 1987).

(*Received* 14 *October* 1987)